Packing microstructures and thermal properties of compressed emulsions: Effect of droplet size

Hsin-Yu Chang [a], Yu-Jane Sheng [a,*], Heng-Kwong Tsao [b,*]

[a] Department of Chemical Engineering, National Taiwan University, Taipei 106, Taiwan
[b] Department of Chemical and Materials Engineering, National Central University, Jhongli 320, Taiwan

ABSTRACT

In preparing thermodynamically metastable emulsions, the droplets tend to coalesce. Consequently, it is difficult to investigate the properties of a monodisperse compressed emulsion experimentally or by simulations. At a specified volume fraction, the properties of emulsions vary with the droplet size but the relevant studies are very limited. The dissipative particle dynamics simulations are adopted to explore the highly concentrated emulsion of monodisperse droplets. Prior knowledge of the microstructure and inter-droplet interaction is not required. The critical packing associated with the onset of the jammed structure can be identified from the growth of the projected area and perimeter of droplets with the volume fraction (ϕ), $\phi_c \approx 0.65$. The mean coordination number ($\underline{Z}$) from the radial distribution function rises with increasing the volume fraction, and can be described by the scaling relation $(\underline{Z}-Z_c) \sim (\phi - \phi_c)^{0.82}$ with $Z_c \approx 6.3$. The effects of the volume fraction, droplet diameter (D), and interfacial tension (σ) on the internal energy ($\underline{U}$) and heat capacity ($\underline{C}_v$) are studied systematically. Both $\underline{U}$ and $\underline{C}_v$ are found to grow as ϕ and σ are increased but D is decreased. According to dimensional analysis, all the data points can be well represented by the scaling relations $(\underline{C}_v - \underline{C}_{v,c}) \sim \phi(\phi - \phi_c)^{1/3}(\sigma/D)$ and $(\underline{U} - \underline{U}_c) \sim \phi(\phi - \phi_c)^{1/3}(\sigma/D)$.

© 2022 Elsevier B.V. All rights reserved.

1. Introduction

An emulsion contains droplets of one liquid dispersed in a second immiscible liquid which is a continuous phase [1]. It is a metastable system and droplet coalescence is impeded by surfactant molecules located at the interface [2]. As the volume fraction of the dispersed phase exceeds about $\phi_c \approx 0.64$, the droplets become crowded and their shapes are deformed from sphere to polyhedron [3–5]. Nonetheless, the dispersed phase is still separated by thin films of the continuous phase. This concentrated system has a large volume of internal (dispersed) phase and is often referred to as high internal phase emulsion (HIPE) [6–9]. For example, the sunflower oil droplets with a 0.94 volume fraction can be stably dispersed in an aqueous solution containing xanthan gum and Tween 20 [10]. Although HIPE is comprised solely of fluids, its rheology is highly unusual and can exhibit elastic behavior at small deformation like solids because of the high degree of crowding. The structural disorder of the droplets is reminiscent of a glass state [1,11].

HIPE is also called the highly concentrated or compressed emulsion and has the characteristics of kinetic stability and mechanical strength [12,13]. The applications of concentrated emulsions include foods, cosmetics, coatings, paints, and pharmaceuticals [14–17]. It can be considered as the solid-like colloidal suspension with the isotropic disordered nonergodic state. The characteristic length of the highly concentrated emulsion is the order of the inter-droplet distance beyond which the static inhomogeneity vanishes. Different from the network gel structure, the elasticity of the concentrated emulsion is originated from the caging (jamming) effect [12]. That is, the constituent droplets of the emulsion are in close contact with each other and the entire system experiences a dynamic arrest. The jamming transition emerging beyond the critical concentration of random close packing can be viewed as a phase transition [18].

The detailed structure of a compressed emulsion is difficult to analyze directly in experiments. Recently, the raw image of a plane in the bulk of polydisperse emulsions was acquired by laser-scanning confocal microscopy with the fluorescent dye. The droplet positions of the marginally jammed system were then reconstructed three-dimensionally by the sphere-matching method. Consequently, the structural characterization of jammed packings can be obtained, including the mean number of neighbors and the radial distribution function g(r) [19].

The physical properties of concentrated emulsions vary significantly with the volume fraction (ϕ) of the dispersed phase. In addition, it is found that the properties such as heat capacity (C_p) and viscosity depend on the size of the droplets (D) significantly in experiments [20–22]. Although the thermophysical property of emulsions was seldom studied, the heat capacity of the concentrated castor oil-in-water emulsions was investigated by differential scanning calorimetry measurement at different emulsification times [23,24]. It is found that the specific heat capacity varies with the surface-to-volume ratio which increases with the emulsification time. In other words, the specific heat capacity grows with the increment of the interfacial area, corresponding to the reduction of droplet sizes at a given ϕ [20].

Highly concentrated emulsions are metastable systems but the spontaneous coalescence between droplets can be impeded by the surfactant layers at the liquid–liquid interfaces. In experimental studies, it is a challenge to acquire concentrated emulsions with a uniform size of droplets. Because of the limitation of preparation techniques and droplet coalescence, the droplet size distribution of the emulsion is generally very broad. As result, the dependence of the emulsion properties on the droplet size is difficult to be accurately investigated from experiments. In contrast, in molecular simulation studies, the droplet size can be easily controlled and thus systematic studies of the influences of droplet size and volume fraction may be achieved. However, in previous simulation studies, the coalescence between droplets is difficult to prevent and the size of the simulated system limits the number of droplets, leading to the inaccuracy of simulation results.

Until now, there are few simulation studies on highly concentrated emulsions. Typically, droplets in emulsions were modeled as assemblies of particles interacting via harmonic pairpotentials to form spring networks [1,25,26]. Because of the limitation of accurate knowledge of microstructures of concentrated emulsions, simple simplifications such as the local coordination number and minimum separation distance are often made [27]. Recently, the microstructure of marginally jammed polydisperse packings has been modeled and agrees excellently with 3D micrographs from experiments on jammed emulsion droplets [19]. In this work, prior knowledge of the microstructure and interdroplet interaction is not required, and the highly concentrated emulsion of monodisperse droplets, whose coalescences are prevented, will be developed in dissipative particle dynamics (DPD) simulations. At a specified volume fraction ($\phi > \phi_c$), the structure evolves toward quasi-equilibrium and the deformed droplets are randomly dispersed in the continuous solvent without controlling the coordination number and minimum separation distance. At quasi-equilibrium, the packing microstructure and thermodynamic properties can be examined. The influences of the volume fraction, droplet size, and interfacial tension are then explored systematically.

2. Method

DPD simulation which is similar to molecular dynamics (MD) is a coarse-grained approach and can overcome the time and space scale limitation in MD [28–32]. A DPD bead with mass m comprises a few atoms or molecules and its motion obeys Newton's equation of motion [33]. The interactions between DPD beads are soft and repulsive and generally contain three types of pairwise-additive and short-ranged forces: conservative force (F_{ij}^C), random force, and dissipative force [34,35]. The equilibrium state is controlled by the conservative force, $F_{ij}^C = a_{ij}(1 - r_{ij} / r_c)\hat{r}_{ij}$, which vanishes as $r_{ij} > r_c$. a_{ij} is the interaction parameter which determines the maximum repulsion. Here r_{ij} represents the distance between the beads i and j, $\hat{r}_{ij}$ the unit vector along the line joining them, r_c

the interaction range. The random force is adopted to control the system temperature T and related to the dissipative force so that the fluctuation–dissipation relation is satisfied [28,30,36,37]. In our simulations, all the mass, length, and energy are nondimensionalized by m, r_c, and k_BT, where k_B denotes the Boltzmann constant.

In this work, the emulsion system contains droplets of the same size dispersed in the continuous phase. Without loss of generality, monodisperse oil droplets are randomly distributed in the water phase initially. For the same types of beads, the interaction parameter a_{ii} is chosen as 25, for example, $a_{oo} = a_{ww} = 25$ for both oil (o) and water (w) phases. For different types of beads, a_{ij} deviates positively from 25 as the incompatibility increases. The interaction parameter between the oil and water phases affects their interfacial tension (σ) and is assumed as $a_{ow} = 50 \sim 80$. For example, as $a_{ow} = 50$, $\sigma = 2.02$ and $a_{ow} = 70$, $\sigma = 3.20$ The thermodynamic instability of emulsions (coalescence of droplets) is generally hindered by the addition of surfactant. However, in this study, the emulsion stability is ensured by introducing a very strong repulsion (e.g., $a_{oo}^* = 3000$) between two touching oil droplets. This assumption is very similar to the strong repulsion between the surfactant layers adsorbed on the two droplets nearly in contact. Note that the simulation result is not sensitive to the value of a_{oo}^* as long as the coalescence can be prevented even in the compressed emulsion. As a result, the deformable droplets remain monodisperse throughout the simulations and all of them contain the same number of DPD beads.

The emulsion was simulated in a cubic box with V = (32.2)³ under periodic boundary conditions subject to the NVT ensemble (constant bead number, simulation box volume, and temperature). The number densities of both dispersed and continuous phases were approximately $\rho \approx 3$ and the total number of DPD beads was N = 100000 [30]. The equation of motion was integrated by the velocity Verlet scheme, and the time increment was set as $\Delta t = 0.01$. The system temperature was always maintained at unity. It took about 3×10^6 steps for the jammed system to reach the quasi-equilibrium state. The volume fraction (ϕ) of the dispersed (oil) phase was defined as the ratio of the total beads in the dispersed phase to those in the system, and it ranged from ϕ = 0.1 to 0.95. The typical snapshots of the emulsion systems were given in Fig. 1 for various volume fractions. The structural characteristics (e.g., the radial distribution function) and thermodynamic properties (e.g., heat capacity) were calculated for quasi-equilibrium emulsions with different volume fractions (ϕ), interfacial tensions (σ), and droplet sizes (D).

The average diameter of the droplet (D) was determined from a few images in the dilute limit where the droplets are nearly spherical, and it was slightly greater than $[n_o/(\rho \times \pi/6)]^{1/3}$, where n_o denotes the number of DPD beads in a droplet. Note that the droplet size (D) can be adjusted by varying n_o. For example, as n_o = 600, D = 7.57 and n_o = 1000, D = 9.27. The average project perimeter (P) and area (A) of the deformed droplet were estimated from a few snapshots over several projections. The structure of a compressed emulsion which is closely associated with the dispersed phase is often realized by the radial distribution function g(r), which described how the droplet density varies as a function of the distance from one particular droplet [38,39]. The radial distribution function of monodisperse droplets is defined as.

$$g(r) = \left(\frac{dn(r)}{4\pi((r + dr)^2 - r^2)} \right) / \rho_d, \tag{1}$$

where dn(r) represents the number of droplets whose centers of mass are located at a distance between r and r + dr from the center of the specified droplet and ρ_d denotes the bulk droplet density which varies with the volume fraction (ϕ) and droplet size (D). The
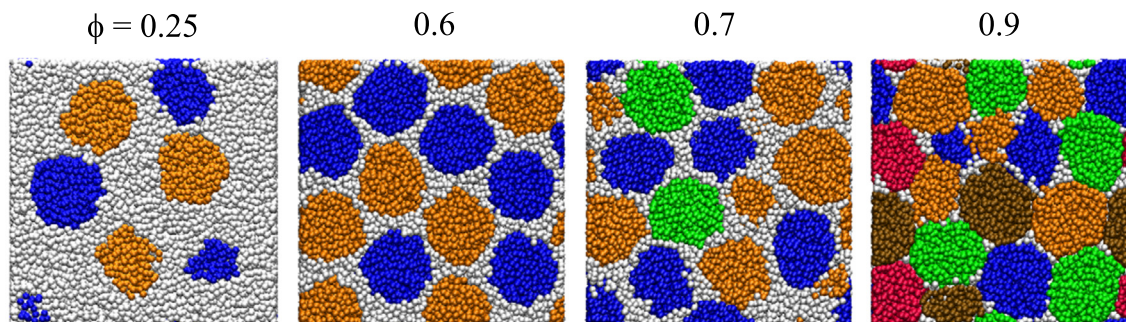
$\phi = 0.25$ 0.6   0.7   0.9

Fig. 1. Snapshots of emulsions at different volume fractions ϕ = 0.25–0.9. The droplets are colored, while the continuous phase is represented by white beads.

mean coordination number ($\underline{Z}$) depicts the average value of the number of the nearest neighboring droplets and it is linked to g(r) directly.

3. Results and discussion

The compressed emulsion in which the volume fraction of the dispersed phase exceeds the critical value (ϕ_c = 0.60 ∼ 0.65) is investigated. In our simulations, the emulsion is always monodisperse and stable because the coalescence between any pair of droplets is completely prevented. The function of the emulsifier which is required to obtain metastable emulsions is simply replaced by the strong short-ranged repulsion between two droplets. Phase inversion which occurs in microemulsions will not take place by adjusting the oil–water ratio. After reaching equilibrium, the microstructure of the jammed system can be analyzed thoroughly and the internal energies can be calculated in details, including those of dispersed phase, continuous phase, and interphase. In this study, both phases are formed by simple liquids such as water and alkane. However, the general influences of the volume fraction, interfacial tension, and droplet size on the behavior of the compressed emulsions are demonstrated and not limited to specific emulsions indicated by the earlier reports [40–42].

3.1. Structure of compressed emulsions

Although the droplet shape fluctuates persistently and the random motion is frequent in the continuous phase, the packing structure of the emulsion can be analyzed statistically. The representative shapes of the droplets which are in the quasi-equilibrium state are demonstrated in Fig. 2(a) for ϕ = 0.85, D = 18.1, and σ = 3.20.

The perimeter and area of the chosen droplets at different times are determined. Note that the perimeter (P) and area (A) are dimensionalized by those of the spherical droplet in the dilute limit (e.g., ϕ = 0.1). As the volume fraction is high, the droplet shape deviates from the sphere evidently and both P and A exceed unity. Some images look like a hexagonal structure. Because of jamming, the mean perimeter and area of a droplet are expected to vary with the volume fraction. Fig. 2(b) shows the variations of P and A with ϕ from 0.1 to 0.95 and the turning points corresponding to the onset of jamming are found to appear at ϕ = ϕ_c≈ 0.65. The perimeter and area were averaged over 100 samples acquired every 1000 time steps. As ϕ < ϕ_c, the slow increment of P and A is accompanied by the shape deformation caused by more collisions between droplets at higher ϕ. The shape deformation grows more significantly with increasing ϕ > ϕ_c, leading to the rapid rise of P and A.

The microstructure of the compressed emulsion can be realized by the radial distribution function g(r), which depicts the probability of finding a droplet from the reference droplet over various dis-

placements. The typical g(r) of ϕ = 0.8 for D = 7.57 and σ = 3.20 is illustrated in the inset of Fig. 3. The first peak is located at r = 6.75, which is less than D = 7.57, indicating that droplets are crowded and deformed significantly. Because of the deformable nature of the droplet and nearly incompressible condition, g(r) drops to zero between the first and second peaks. The influence of the volume fraction ϕ on the position of the first peak is shown in Fig. 3. As ϕ is decreased, the position of the first peak is generally increased and close to the droplet diameter D. This consequence can be understood from the fact that lower volume fractions yield less jammed configurations.
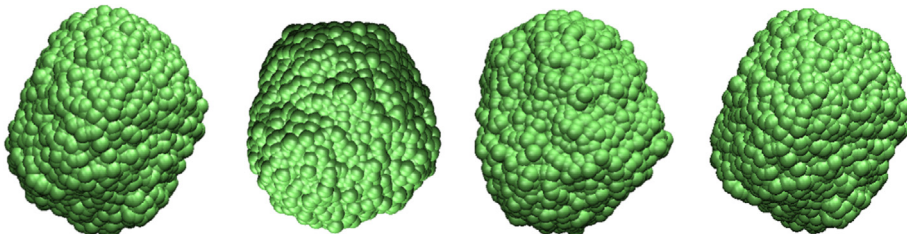
The distribution of the distance between the centers of two neighboring droplets is closely related to the first peak of g(r). Note that two neighboring soft droplets do not necessarily contact each other in the compressed emulsion. A representative cross-section picture is demonstrated in Fig. 4, and it shows that the centered droplet is either in direct contact with the nearby droplet or separated from the neighboring droplet by a thin water layer. The mean distance r_m and standard deviation (SD) are expected to vary with the volume fraction. As anticipated, Fig. 4 with D = 7.57 shows that the mean distance declines with increasing ϕ. However, the standard deviation of the distance distribution is found to grow with increasing ϕ, as depicted in the inset. This result reveals that the greater shape deformation associated with larger ϕ leads to the wider distribution of the distance between neighboring droplets. Since the standard deviation is much smaller than the droplet size, the nearly incompressible condition is still fulfilled.

The feature of the first shell around a center droplet can be described by the coordination number, which varies with the position and depends on the volume fraction as well. Fig. 5(a) demonstrates the probability distribution of the coordination number (Z) for different values of ϕ with D = 7.57. As ϕ is increased, the distribution shifts to the large Z and becomes narrower. The largest coordination number can reach 18 at ϕ = 0.95. As shown in Fig. 5 (b), the mean coordination number ($\underline{Z}$) grows with increasing ϕ and the turning point can be identified at ϕ_c = 0.65, corresponding to the onset of droplet jamming. For ϕ > ϕ_c, the rapid rise of $\underline{Z}$ is accompanied with serious shape deformation. The relation between the mean coordination number and volume fraction may be depicted by the power law $(\underline{Z} - Z_c) \sim (\phi - \phi_c)^{\alpha}$ [18,27], where Z_c is $\underline{Z}$ at ϕ = ϕ_c. The inset of Fig. 5(b) shows a linear line with the slope α = 0.82 in the logarithmic plot of $(\underline{Z} - Z_c)$ against $(\phi - \phi_c)$ for ϕ > ϕ_c, which is slightly greater than the value reported in literature 0.5 obtained soft sphere simulations based on the network spring model [27].

3.2. Internal **energy and heat capacity**

In previous simulation studies [1,27], the internal energy of the compressed emulsion which is a disordered droplet packing has

(a) Typical projected shapes of the droplet

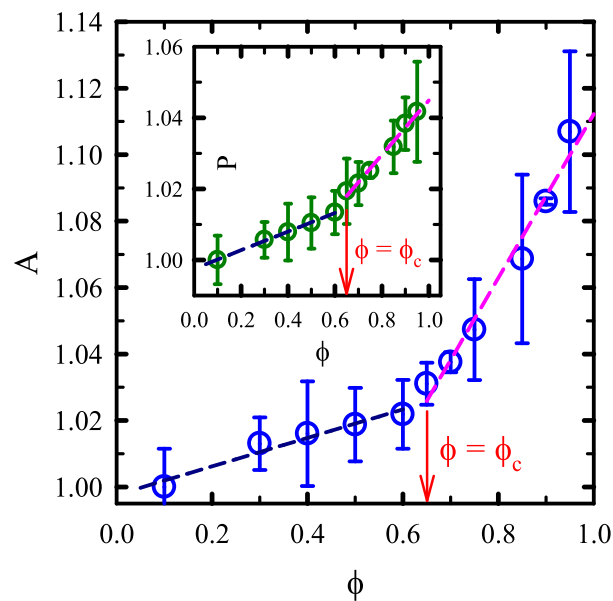| Perimeter (P)	1.04	1.04	1.03	1.02
Area (A)	1.07	1.06	1.06	1.07
Snapshot				
	(t = 30000)	(t = 28000)	(t = 25000)	(t = 24000)

(b) Effect of the volume fraction

Fig. 2. (a) The dimensionless projected perimeter (P) and area (A) associated with the typical droplet shown in the snapshots for $\phi = 0.85$, $D = 18.1$, and $\sigma = 3.20$. P and A are scaled by those of droplets in the dilute limit. (b) The variation of the mean perimeter and area with the volume fraction. The turning point gives the critical volume fraction $\phi_c \approx 0.65$.

been modeled as a system of soft spheres which interact with their nearest neighbors. The repulsive central-force potential such as harmonic-spring potential is frequently adopted to reflect the behavior of facets. As a result, the details of the shape response to deformation and the coupling between different facets on each droplet are ignored. Based on the average coordination number and a single effective potential, the internal energy of the system becomes tractable, as the forces acting on each droplet are balanced. In this work, however, the stable compressed emulsion is simulated without assuming the interdroplet interaction potential. As the droplets are compressed, the changes in interfacial energy are accounted for directly and the effects of the volume fraction,

droplet size, and interfacial tension on the internal energy can be calculated.

The internal energy (U) of the emulsion is separated into three contributions: dispersed phase (U_d), continuous phase (U_c), and interface (U_i). The total energy of the system is $U = U_d + U_c + U_i$ where U_i represents the sum of the pair potentials between oil and water beads at contacts. The internal energy per bead is denoted by $\underline{U}_k$ ($k = c$, d, or i) and $\underline{U}_i$ is U_i divided by the number of beads in the dispersed phase which are in contact with the continuous phase. Fig. 6 shows the variation of the internal energy with the volume fraction of the dispersed phase for the droplet diameter $D = 9.27$ and interfacial tension $\sigma = 3.20$. Evidently, near
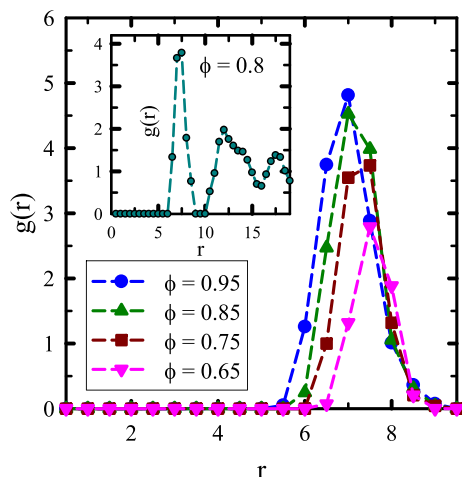
Fig. 3. The short-range radial distribution function g(r) for the monodisperse compressed emulsions with D = 7.57 and σ = 3.20 at volume fractions from 0.65 to 0.95. In the inset, the typical radial distribution function g(r) for φ = 0.8 is demonstrated.
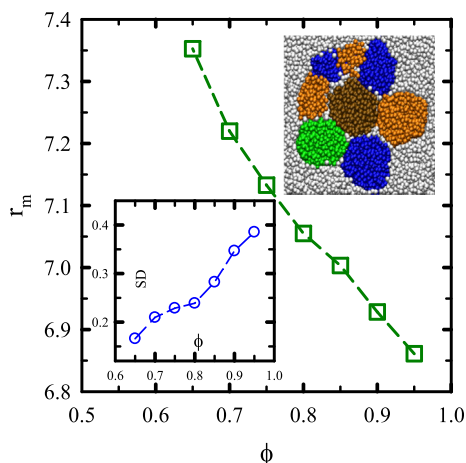

Fig. 4. The mean distance between two neighboring droplets (r_m) is plotted against the volume fraction at D = 7.57 and σ = 3.2. The lower inset shows the standard deviation (SD) of the distribution of the interdroplet distance. In the upper inset, the snapshot illustrates the neighboring droplets surrounding the central droplet.

(a) Distribution of the coordination number

(b) Effect of the volume fraction

Fig. 5. (a) The probability distribution of the coordination number (Z) with D = 7.57 and σ = 3.20 for different values of φ. The sum of the distribution equals unity. (b) The variation of the mean coordination number ($\underline{Z}$) with the volume fraction. In the inset, ($\underline{Z} - Z_c$) is plotted logarithmically against ($\phi - \phi_c$) and the data points can be represented by the linear line with the slope of 0.82.

the critical volume fraction, $\underline{U}_c$ decreases fast while $\underline{U}_i$ ascends rapidly. Without loss of generality, the continuous phase is assumed as water and the dispersed phase is oil for simplicity. As $\phi - \phi_c$ is increased, the average number of oil beads in contact with each water bead rises, leading to the rapid growth of $\underline{U}_i$. In contrast, the number of water-water pairs per water bead decreases accordingly, resulting in the sharp decrement of $\underline{U}_c$. In addition to the changes of $\underline{U}_i$ and $\underline{U}_c$, $\underline{U}_d$ is also found to vary with φ, as shown in the inset of Fig. 6. For $\phi < \phi_c$, the linear increase of $\underline{U}_d$ with φ is associated with the growth of the osmotic pressure. For $\phi > \phi_c$, the increment of $\underline{U}_d$ is attributed to the internal pressure buildup due to the jamming structure. The turning point at $\phi = \phi_c$ reflects the two different mechanisms. Note that the contribution of direct contacts between two droplets to the total internal energy is negligible (about 0.08 %).

In addition to φ, the internal energy per bead ($\underline{U}$) of the compressed emulsion depends on σ and D as well. Fig. 7(a) shows the variation of the internal energy contributions with the interfacial tension at the volume fraction φ = 0.8 and droplet size D = 8.6. As σ is increased, the water bead disfavors the oil bead more, facil-

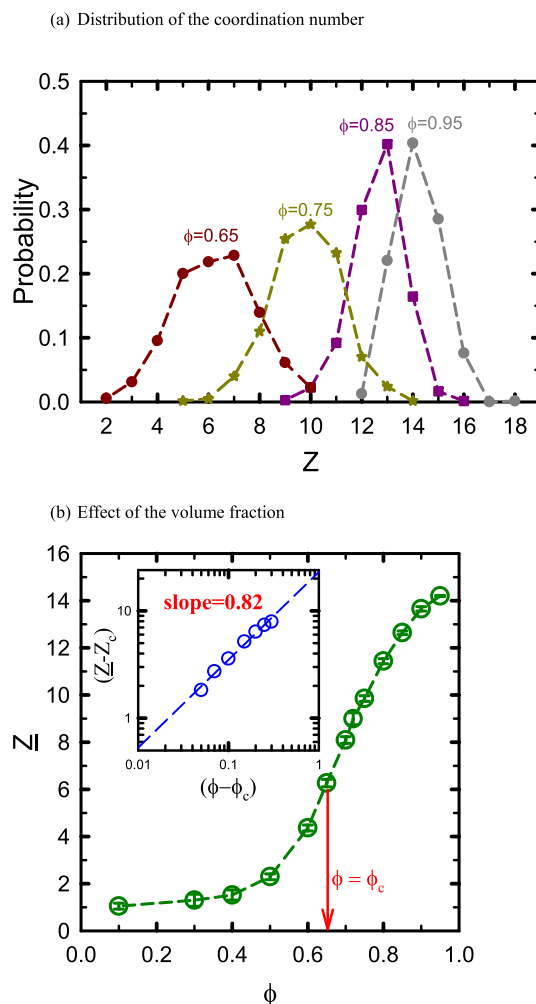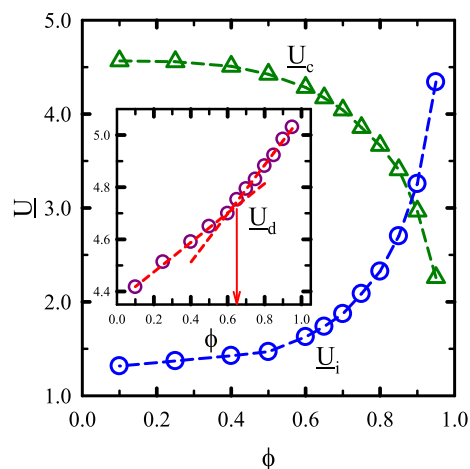**Fig. 6.** The variation of the internal energy associated with the continuous phase ($\underline{U}_c$) and interface ($\underline{U}_i$) with the volume fraction for D = 9.27 and σ = 3.20. In the inset, the internal energy of the dispersed phase ($\underline{U}_d$) is plotted against the volume fraction.

itating the contacts between water beads. Therefore, $\underline{U}_i$ (interface) decreases but $\underline{U}_c$ (water phase) ascends. Besides, $\underline{U}_d$ (oil phase) is also found to grow with increasing σ. This result is accompanied by the increment of the pressure inside the droplet based on the Young-Laplace equation ($P_d = P_c + 4\sigma/D$). Fig. 7(b) shows the variation of the internal energy contributions with the droplet diameter (D) at $\phi = 0.8$ and $\sigma = 3.20$. As D is decreased from 17.21 to 6.83, the interfacial area increases, and therefore $\underline{U}_i$ grows accordingly. It is somewhat surprising to find the increment of $\underline{U}_d$ and the slight decline of $\underline{U}_c$ with decreasing the droplet size. According to the Young-Laplace equation ($\Delta P = 4\sigma/D$), either P_d (dispersed phase) ascends or P_c (continuous phase) descends, as D is decreased [43–45]. The rise of P_d results in the decrease of the mean distance between beads, leading to the growth of $\underline{U}_d$. In contrast, the fall of P_c gives the decrease of $\underline{U}_c$.

The heat capacity C_v is important for applications involving heating or cooling processes, and it describes the amount of ther-

mal energy required to raise the temperature of the system by one degree. However, very few studies report the thermophysical property such as heat capacity of emulsions. By using a differential-scanning-calorimetry technique, the specific heat capacity of highly concentrated castor oil-in-water emulsions (more than 90 % oil) was obtained [20]. It is found that at a given composition, the heat capacity grows with the emulsification time which affects the mean droplet size. Short emulsification times give more polydisperse emulsions with bigger droplets. That is, the heat capacity of emulsions varies with the emulsion morphology or mean droplet size [20]. This result is interesting because the thermophysical property of a mixture is generally expected to depend on the composition only. To eliminate the effect of polydispersity, concentrated emulsions of monodisperse droplets are considered to evaluate the internal energies and specific heat capacities in our simulations.

The specific heat capacity can be determined by the fluctuation of the internal energy [46],

$$Cv = \left(\frac{\partial U}{\partial T}\right)_V = \frac{<U^2> - <U>^2}{k_B T^2} \tag{2}$$

$\underline{U}^2$ and $\underline{U}$ are recorded every 100 DPD steps during the simulation. According to the results of the internal energy, the heat capacity of the emulsion system has to vary with the droplet size (D) and interfacial tension (σ) as well, in addition to the composition (ϕ). As demonstrated in the inset of Fig. 8, $\underline{U}$ grows with increasing the volume fraction (ϕ) for D = 7.57 and $\sigma = 3.20$. It seems that there exists a turning point at $\phi \approx 0.65$ although the difference between the slopes (0.72 and 0.82) is not significant. The transition from the free movement of droplets to the jammed structure is more eminent in the plot of the heat capacity against the volume fraction (Fig. 8). The sharp change of $\underline{C}_v$ for D = 7.57 can be clearly seen in the regime $\phi = 0.6 \sim 0.7$, indicating the structural transition associated with the emergence of the jamming.

Because the internal energy is a function of $\underline{U}(\phi,\sigma,D)$, the heat capacity is also a function of $\underline{C}_v(\phi,\sigma,D)$. The variation of $\underline{C}_v$ with σ for $\phi = 0.8$ and D = 8.6 is illustrated in the inset of Fig. 9. Obviously, $\underline{C}_v$ grows linearly with σ although the interfacial interaction energy $\underline{U}_i$ decreases with increasing σ (see Fig. 7(a)). In fact, $\underline{U}$ is also found to grow linearly with σ, indicating that $\underline{U}_c$ and $\underline{U}_d$ dom-

(a) Effect of the interfacial tension
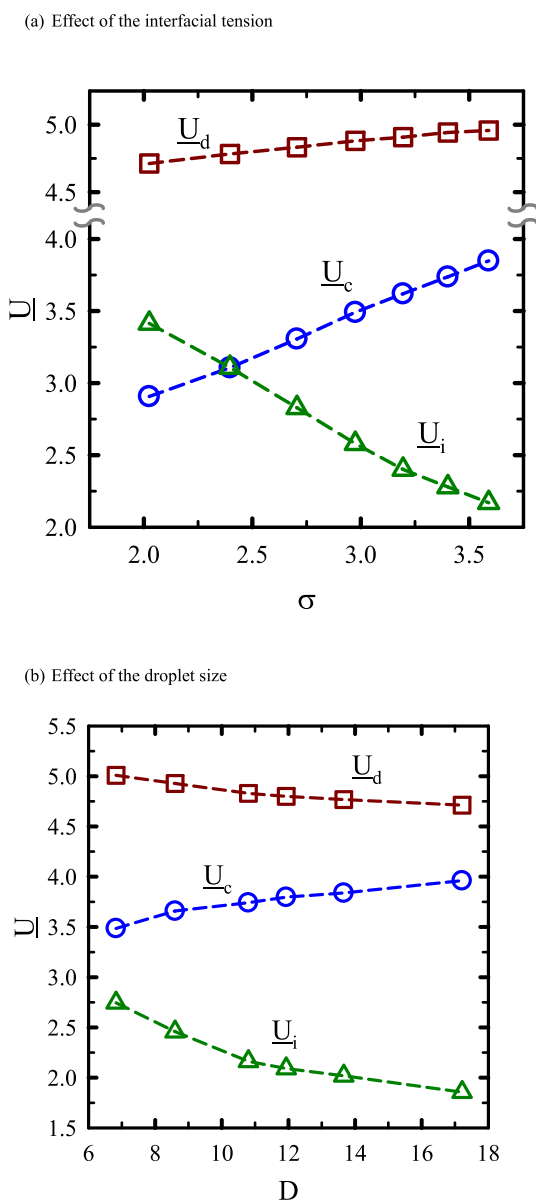

(b) Effect of the droplet size

Fig. 7. (a) The variation of the internal energy ($\underline{U}_c$, $\underline{U}_d$, and $\underline{U}_i$) with the interfacial tension for $\phi = 0.8$ and D = 8.6. (b) The variation of the internal energy with the droplet size for $\phi = 0.8$ and $\sigma = 3.20$.
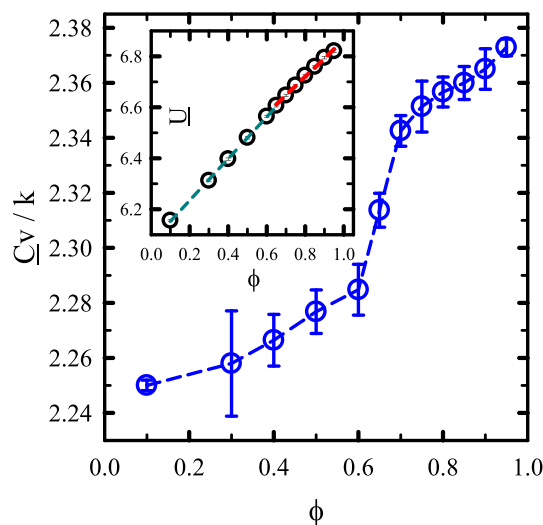

Fig. 8. The heat capacity $\underline{C}_v$ is plotted against the volume fraction for D = 7.57 and $\sigma = 3.20$. The inset shows that the internal energy per bead ($\underline{U}$) is plotted against the volume fraction.
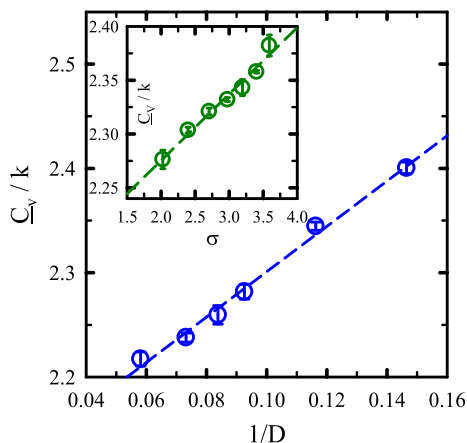
Fig. 9. The heat capacity ($\underline{C}_v$) is plotted against the reciprocal of the droplet size (1/D) for $\phi = 0.8$ and $\sigma = 3.20$. The inset shows that the heat capacity ($\underline{C}_v$) is plotted against the interfacial tension for $\phi = 0.8$ and $D = 8.6$.

inate the change of $\underline{U}$ with σ. The variation of $\underline{C}_v$ with 1/D for $\phi = 0.8$ and $\sigma = 3.20$ is shown in Fig. 9. Again, $\underline{C}_v$ grows linearly with 1/D, which is consistent with the decrement of $\underline{U}_i$ and $\underline{U}_d$ with D (see Fig. 7(b)). Note that $\underline{U}$ grows linearly with 1/D, revealing that $\underline{U}_i$ and $\underline{U}_d$ dominate the change of $\underline{U}$ with D. Because the interfacial area increases and the buildup of the Laplace pressure with 1/D, $\underline{U}_i$, and $\underline{U}_d$ prevail over the linear change of $\underline{U}_c$ with 1/D. The results shown in Fig. 9 for $\phi = 0.8$ demonstrate that $\underline{C}_v$ is proportional to both σ and 1/D for $\phi \geq \phi_c$. Moreover, it is not surprising to observe that $\underline{U}$ is proportional to both σ and 1/D for $\phi \geq \phi_c$ as well.

$\underline{U}$ and $\underline{C}_v$ are a function of ϕ, σ, and D because of the existence of the interfaces in emulsions. The above findings and dimensional analysis reveal that $\rho\underline{C}_v$ and $\rho\underline{U}$ may be a linear function of σ/D, where the density is $\rho = 3$ in this work. Fig. 10(a) shows the variation of $\underline{C}_v$ and $\underline{U}$ with σ/D for different combinations of σ and D at $\phi = 0.8$. All data points are collapsed reasonably into a single line, indicating the linear relationship between $\underline{C}_v$ (or $\underline{U}$) and σ/D. The dependence of the physical quantities on ϕ for compressed emulsions are often described by $\phi^\alpha(\phi - \phi_c)^\beta$ [1,3,47]. As a result, the contribution at $\phi = \phi_c$ must be eliminated and the relations between $\Delta\underline{U} = \underline{U}(\phi) - \underline{U}(\phi_c)$ or $\Delta\underline{C}_v = \underline{C}_v(\phi) - \underline{C}_v(\phi_c)$ and ϕ are considered. Fig. 10(b) shows the plots of $\Delta\underline{C}_v/(\sigma/D)$ and $\Delta\underline{U}/(\sigma/D)$ against $\phi(\phi - \phi_c)^{1/3}$ for various combinations of ϕ, σ, and D. Again, all data points are collapsed reasonably into a single line, revealing that $\Delta\underline{C}_v$ and $\Delta\underline{U}$ are linearly proportional to $\phi(\phi - \phi_c)^{1/3}(\sigma/D)$.

4. Conclusion

The emulsion is thermodynamically metastable because the droplets stabilized by adsorbed surfactant tend to coalesce with time. As a result, it is difficult to investigate the properties of a monodisperse compressed emulsion experimentally or by simulations. Even subject to a specified volume fraction, the influence of the droplet size is significant but still not clear. In this work, DPD simulations are employed to study the compressed emulsion in which the monodisperse droplets are jammed but their coalescences are completely prevented. At quasi-equilibrium, the microstructures of the compressed emulsions are examined for various volume fractions (ϕ). By analyzing the growth of the projected area and perimeter of droplets with ϕ, the critical volume fraction corresponding to the turning point is identified as $\phi_c \approx 0.65$. Moreover, the radial distribution function and the coordination number from a reference droplet are acquired. As the vol-
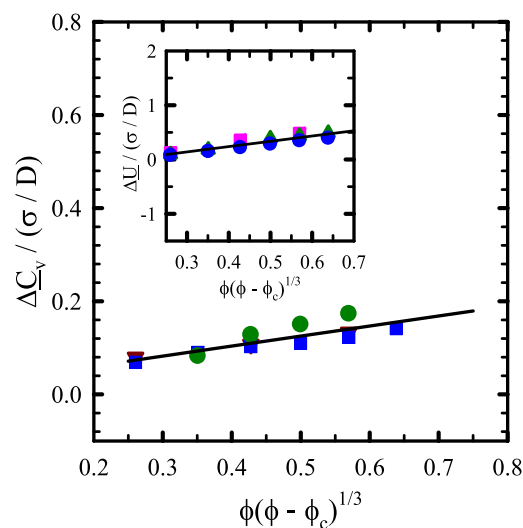
(a) Function of σ/D
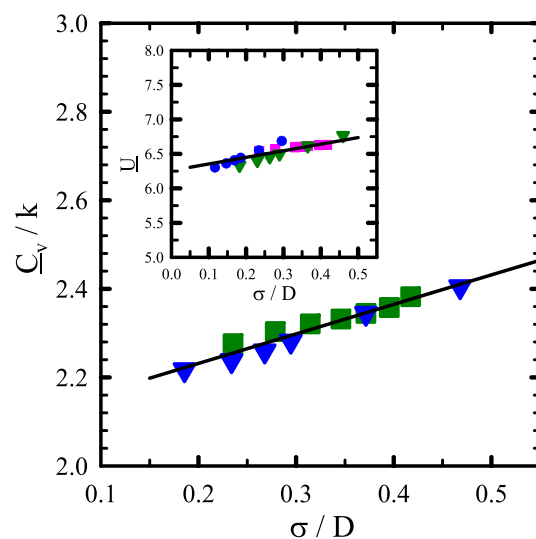
(b) Function of (ϕ - ϕ_c)

Fig. 10. (a) The plots of $\underline{C}_v$ and $\underline{U}$ against σ/D for various combinations of σ and D at $\phi = 0.8$. (b) The plots of $\Delta\underline{C}_v/(\sigma/D)$ and $\Delta\underline{U}/(\sigma/D)$ against $\phi(\phi - \phi_c)^{1/3}$ for various combinations of ϕ, σ, and D. All data points can collapse into a linear line reasonably.

ume fraction increases, it is found that the mean coordination number ($\underline{Z}$) rises and can be described by the scaling relation ($\underline{Z} - Z_c$) $\sim$ ($\phi - \phi_c$)$^{0.82}$ with $Z_c \approx 6.3$.

The internal energy per bead ($\underline{U}$) and heat capacity ($\underline{C}_v$) of compressed emulsions are evaluated as well and the effects of the volume fraction, droplet diameter (D), and interfacial tension (σ) are examined. To analyze the underlying mechanism, $\underline{U}$ is separated into three contributions: continuous phase $\underline{U}_c$, dispersed phase $\underline{U}_d$, and interface $\underline{U}_i$. As ϕ is increased or D is decreased, $\underline{U}$ rises because both $\underline{U}_d$ and $\underline{U}_i$ increase. The increment of $\underline{U}_d$ is associated with the buildup of the Laplace pressure, while the increment of $\underline{U}_i$ is accompanied with the growth of the interfacial area. As σ is increased, $\underline{U}$ ascends but $\underline{U}_i$ is found to decay surprisingly. The change in $\underline{U}$ is attributed to the growths of both $\underline{U}_d$ and $\underline{U}_c$ associ-

ated with the increment of the Laplace pressure. The dependence of the heat capacity on ϕ, D, and σ is the same as the internal energy. According to the dimensional analysis, all the data points can be well represented by the scaling relations $(\underline{C}_v - \underline{C}_{v,c}) \sim \phi(\phi - \phi_c)^{1/3}(\sigma/D)$ and $(\underline{U} - \underline{U}_c) \sim \phi(\phi - \phi_c)^{1/3}(\sigma/D)$. In addition to structural and thermodynamic properties, our new simulation approach can be applied to explore the mechanical and viscoelastic properties of compressed emulsions, which are currently under study.

CRediT authorship contribution statement

Hsin-Yu Chang: Investigation, Methodology, Formal analysis, Data curation, Writing – original draft. **Yu-Jane Sheng:** Funding acquisition, Supervision, Resources, Writing – review & editing. **Heng-Kwong Tsao:** Conceptualization, Funding acquisition, Supervision, Resources, Writing – review & editing.

Data availability

Data will be made available on request.

Declaration of Competing Interest

The authors declare that they have no known competing financial interests or personal relationships that could have appeared to influence the work reported in this paper.

Acknowledgment

References

[1] T.G. Mason, J. Bibette, D.A. Weitz, Elasticity of compressed emulsions, Phys. Rev. Lett. 75 (10) (1995) 2051–2054.

[2] C.-Y. Lu, J. Yu, Dielectric response of a dilute oil-in-water emulsion solution, Chin. J. Phys. 40 (1) (2002) 60–68.

[3] H. Princen, A. Kiss, Rheology of foams and highly concentrated emulsions: III. Static shear modulus, J. Colloid Interface Sci. 112 (2) (1986) 427–437.

[4] S. Torquato, T.M. Truskett, P.G. Debenedetti, Is random close packing of spheres well defined?, Phys Rev. Lett. 84 (10) (2000) 2064–2067.

[5] R. Foudazi, S. Qavi, I. Masalova, A.Y. Malkin, Physical chemistry of highly concentrated emulsions, Adv. Colloid Interface Sci. 220 (2015) 78–91.

[6] T. Zhang, R.A. Sanguramath, S. Israel, M.S. Silverstein, Emulsion templating: porous polymers and beyond, Macromolecules 52 (15) (2019) 5445–5479.

[7] S.-W. Hu, P.-J. Sung, T.P. Nguyen, Y.-J. Sheng, H.-K. Tsao, UV-Resistant Self-Healing Emulsion Glass as a New Liquid-like Solid Material for 3D Printing, ACS Appl. Mater. Interfaces 12 (21) (2020) 24450–24457.

[8] V.G. Babak, M.-J. Stébé, Highly concentrated emulsions: physicochemical principles of formulation, J. Dispers. Sci. Technol. 23 (1–3) (2002) 1–22.

[9] G. Sun, Z. Li, T. Ngai, Inversion of particle-stabilized emulsions to form high-internal-phase emulsions, Angew. Chem. 122 (12) (2010) 2209–2212.

[10] H. Tan, G. Sun, W. Lin, C. Mu, T. Ngai, Gelatin particle-stabilized high internal phase emulsions as nutraceutical containers, ACS Appl. Mater. Interfaces 6 (16) (2014) 13977–13984.

[11] T.P. Nguyen, S.-W. Hu, Y.-J. Lin, Y.-J. Sheng, H.-K. Tsao, Coexistence of liquid-like emulsion and solid-like emulsion glass beyond the close-packing limit, J. Taiwan Inst. Chem. Eng. 115 (2020) 28–34.

[12] T.P. Nguyen, S.-W. Hu, Y.-J. Sheng, H.-K. Tsao, Scanty-water oil-in-water emulsion glasses synthesized through a low-energy process: Nucleation and growth mechanism, J. Taiwan Inst. Chem. Eng. 109 (2020) 129–136.

[13] D. Langevin, S. Poteau, I. Hénaut, J. Argillier, Crude oil emulsion properties and their application to heavy oil transportation, Oil Gas Sci. Technol. 59 (5) (2004) 511–521.

[14] N.R. Cameron, High internal phase emulsion templating as a route to well-defined porous polymers, Polymer 46 (5) (2005) 1439–1449.

[15] J. Bibette, D.C. Morse, T.A. Witten, D.A. Weitz, Stability criteria for emulsions, Phys. Rev. Lett. 69 (16) (1992) 2439–2442.

[16] A. Speltini, G. Tripodo, F. Rinaldi, G. Massolini, A. Profumo, E. Calleri, Carbon nanotubes-modified poly-high internal phase emulsions for pharmaceuticals pre-concentration and determination, J. Pharm. Biomed. Anal. 207 (2022) 114391.

[17] E.M. Shchukina, D.G. Shchukin, Layer-by-layer coated emulsion microparticles as storage and delivery tool, Curr. Opin. Colloid Interface Sci. 17 (5) (2012) 281–289.

[18] H. Zhang, H. Makse, Jamming transition in emulsions and granular materials, Phys. Rev. E 72 (1) (2005) 011301.

[19] C. Zhang, C.B. O'Donovan, E.I. Corwin, F. Cardinaux, T.G. Mason, M.E. Möbius, F. Scheffold, Structure of marginally jammed polydisperse packings of frictionless spheres, Phys. Rev. E 91 (3) (2015) 032302.

[20] A. Jamil, S. Caubet, B. Grassl, T. Kousksou, K. El Omari, Y. Zeraouli, Y. Le Guer, Thermal properties of non-crystallizable oil-in-water highly concentrated emulsions, Colloids Surf. A Physicochem. Eng. Asp. 382 (1–3) (2011) 266–273.

[21] R. Pal, A novel method to correlate emulsion viscosity data, Colloids Surf. A Physicochem. Eng. Asp. 137 (1–3) (1998) 275–286.

[22] P. Partal, A. Guerrero, M. Berjano, C. Gallegos, Influence of concentration and temperature on the flow behavior of oil-in-water emulsions stabilized by sucrose palmitate, J. Am. Oil Chem. Soc. 74 (10) (1997) 1203–1212.

[23] K. Jørgensen, Calorimetric detection of a sub-main transition in long-chain phosphatidylcholine lipid bilayers, Biochim. Biophys. Acta Biomembr. 1240 (2) (1995) 111–114.

[24] D. Clausse, F. Gomez, I. Pezron, L. Komunjer, C. Dalmazzone, Morphology characterization of emulsions by differential scanning calorimetry, Adv. Colloid Interface Sci. 117 (1–3) (2005) 59–74.

[25] J. Brujić, S.F. Edwards, D.V. Grinev, I. Hopkinson, D. Brujić, H.A. Makse, 3D bulk measurements of the force distribution in a compressed emulsion system, Faraday Discuss. 123 (2003) 207–220.

[26] T. Mason, M.-D. Lacasse, G. Grest, D. Levine, J. Bibette, D. Weitz, Osmotic pressure and viscoelastic shear moduli of concentrated emulsions, Phys. Rev. E 56 (3) (1997) 3150–3166.

[27] M.-D. Lacasse, G.S. Grest, D. Levine, T.G. Mason, D.A. Weitz, Model for the elasticity of compressed emulsions, Phys. Rev. Lett. 76 (18) (1996) 3448–3451.

[28] P. Español, P. Warren, Statistical mechanics of dissipative particle dynamics, EPL 30 (4) (1995) 191–196.

[29] P.J. Hoogerbrugge, J.M.V.A. Koelman, Simulating microscopic hydrodynamic phenomena with dissipative particle dynamics, EPL 19 (3) (1992) 155–160.

[30] R.D. Groot, P.B. Warren, Dissipative particle dynamics: Bridging the gap between atomistic and mesoscopic simulation, J. Chem. Phys. 107 (11) (1997) 4423–4435.

[31] A.F. Jakobsen, Constant-pressure and constant-surface tension simulations in dissipative particle dynamics, J. Chem. Phys. 122(12) (2005) 124901.

[32] T.-Y. Wang, H.-K. Tsao, Y.-J. Sheng, Perforated Vesicles of ABA Triblock Copolymers with ON/OFF-Switchable Nanopores, Macromolecules 53 (23) (2020) 10582–10590.

[33] K.-C Huang, C.-M. Lin, H.-K. Tsao, Y.-J. Sheng, The interactions between surfactants and vesicles: Dissipative particle dynamics, J. Chem. Phys. 130 (24) (2009) 06B622.

[34] Y.-L. Yang, Y.-J. Sheng, H.-K. Tsao, Hybridization of lipids to monolayer and bilayer membranes of triblock copolymers, J. Colloid Interface Sci. 544 (2019) 53–60.

[35] Y.-S. Peng, Z. Wang, K.-C. Chu, Y.-J. Sheng, H.-K. Tsao, Favorable partition of nanoswimmers toward a confined slit, Phys. Rev. E 100 (4) (2019) 042604.

[36] I. Pagonabarraga, M.H.J. Hagen, D. Frenkel, Self-consistent dissipative particle dynamics algorithm, EPL 42 (4) (1998) 377–382.

[37] H.-Y. Chang, P.-H. Chiu, H.-K. Tsao, Y.-J. Sheng, Strengthening mechanism of the mechanical properties of graft copolymers with incompatible pendant groups: nano-clusters and weak cross-linking, Soft Matter 17 (23) (2021) 5730–5737.

[38] Y.-L. Lin, C.-S. Chiou, S.K. Kumar, J.-J. Lin, Y.-J. Sheng, H.-K. Tsao, Self-assembled superstructures of polymer-grafted nanoparticles: effects of particle shape and matrix polymer, J. Phys. Chem. C 115 (13) (2011) 5566–5577.

[39] S.-W. Hu, Y.-J. Sheng, H.-K. Tsao, Self-assembly of organophilic nanoparticles in a polymer matrix: Depletion interactions, J. Phys. Chem. C 116 (2) (2012) 1789–1797.

[40] F. Alvarez, E. Flores, L. Castro, J. Hernández, A. López, F. Vazquez, Dissipative particle dynamics (DPD) study of crude oil− water emulsions in the presence of a functionalized co-polymer, Energy fuels 25 (2) (2011) 562–567.

[41] J. Zhang, L. Chen, A. Wang, Z. Yan, Dissipative particle dynamics simulation of ionic liquid-based microemulsion: Quantitative properties and emulsification mechanism, Ind. Eng. Chem. Res. 59 (2) (2019) 763–773.

[42] M. Li, H. Zhang, Z. Wu, Z. Zhu, X. Jia, DPD Simulation on the Transformation and Stability of O/W and W/O Microemulsions, Molecules 27 (4) (2022) 1361.

[43] K.-C. Chu, H.-K. Tsao, Y.-J. Sheng, Pressure-gated capillary nanovalves based on liquid nanofilms, J. Colloid Interface Sci. 560 (2020) 485–491.

[44] H. Liu, G. Cao, Effectiveness of the Young-Laplace equation at nanoscale, Sci. Rep. 6 (1) (2016) 1–10.

[45] M. Matsumoto, K. Tanaka, Nano bubble−Size dependence of surface tension and inside pressure, Fluid Dyn. Res. 40 (7-8) (2008) 546–553.

[46] H.-L. Wu, Y.-J. Sheng, H.-K. Tsao, Phase behaviors and membrane properties of model liposomes: Temperature effect, J. Chem. Phys. 141 (12) (2014) 09B619_1.

[47] I. Masalova, A.Y. Malkin, Rheology of highly concentrated emulsions– Concentration and droplet size dependencies, Appl. Rheol. 17(4) (2007) 42250-1-42250-9.